Leapfrog Cracking and Nanoamorphization of ZnO Nanowires during In Situ Electrochemical Lithiation

Akihiro Kushima,[†] Xiao Hua Liu,[‡] Guang Zhu,[§] Zhong Lin Wang,[§] Jian Yu Huang,*[‡] and Ju Li*[†,||]

[†]Department of Materials Science and Engineering, University of Pennsylvania, Philadelphia, Pennsylvania 19104, United States

[‡]Center for Integrated Nanotechnologies, Sandia National Laboratories, Albuquerque, New Mexico 87185, United States

[§]School of Materials Science and Engineering, Georgia Institute of Technology, Atlanta, Georgia 30332-0245, United States

[||]State Key Laboratory for Mechanical Behavior of Materials and Frontier Institute of Science and Technology, Xi'an Jiaotong University, Xi'an, 710049, China

ⓢ Supporting Information

ABSTRACT: The lithiation reaction of single ZnO nanowire (NW) electrode in a Li-ion nanobattery configuration was observed by in situ transmission electron microscopy. Upon first charge, the single-crystalline NW was transformed into a nanoglass with multiple glassy nanodomains (Gleiter, H. *MRS Bulletin* **2009**, *34*, 456) by an intriguing reaction mechanism. First, partial lithiation of crystalline NW induced multiple nanocracks ∼70 nm ahead of the main lithiation front, which traversed the NW cross-section and divided the NW into multiple segments. This was followed by rapid surface diffusion of Li⁺ and solid-state amorphization along the

open crack surfaces. Finally the crack surfaces merged, leaving behind a glass—glass interface (GGI). Such reaction front instability also repeated in the interior of each divided segment, further subdividing the NW into different nanoglass domains (nanoamorphization). Instead of the profuse dislocation plasticity seen in SnO_2 NWs (*Science* **2010**, *330*, 1515), no dislocation was seen and the aforementioned nanocracking was the main precursor to the electrochemically driven solid-state amorphization in ZnO. Ab initio tensile decohesion calculations verified dramatic lithium embrittlement effect in ZnO, but not in SnO_2. This is attributed to the aliovalency of Sn cation (Sn(IV), Sn(II)) in contrast to the electronically more rigid Zn(II) cation.

KEYWORDS: Nanoglass and nanoamorphization, crack, lithium embrittlement, in situ TEM, lithium ion battery (LIB) decrepitation, glass—glass interface (GGI) memory effect
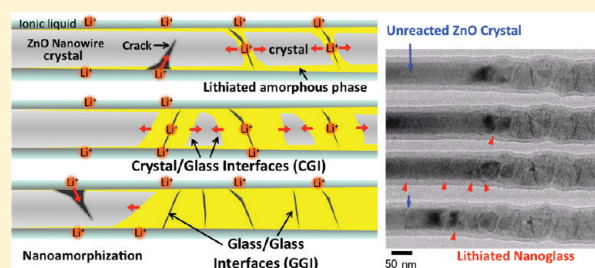
Lithium ion batteries (LIBs) are leading candidates for electric-vehicle applications where high power, energy capacity, and cyclability are required. Nanowire electrodes[1−6] may offer some significant advantages over conventional electrodes due to the unique structures of NWs that facilitate electron and Li⁺ transport, and the ability to accommodate large volume change during charge/discharge cycles.[2,5,7,8] Further, the electron transparency of NWs allows one to perform in situ transmission electron microscopy (TEM) observations of the microstructural evolution during lithiation/delithiation, using a new technique we developed recently.[9] The real time observation of the charge/discharge process of NW electrodes in a Li-ion battery can provide insights into the reaction mechanism at nanoscale, guiding the development of advanced LIBs with improved power, energy density, and lifetime.[10] As an application of this technique, the detailed pathways of electrochemically driven solid-state amorphization (ESSA)[11] can now be examined at an unprecedented spatial

and temporal resolution. In this context, we used ZnO NWs as the anode to observe in real time the electrochemical reaction

$$(2 + x)e^- + ZnO + (2 + x)Li^+ = Li_2O + Li_xZn \qquad (1)$$
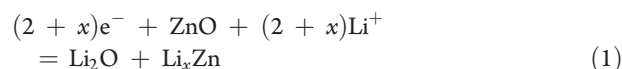
as a contrast to SnO_2,[9] another well-studied oxide NW. The theoretical capacity of ZnO is 978 mAh/g, which is nearly three times higher than that of graphite (372 mAh/g), the commonly used anode in LIBs. But bulk ZnO shows very poor cyclability.[12−14] The nanostructured ZnO is reported to have improved cyclability.[15] However, the detailed lithiation mechanism of neither bulk nor nano ZnO was understood, preventing the application of ZnO as a battery electrode. In addition to the novelty of NW
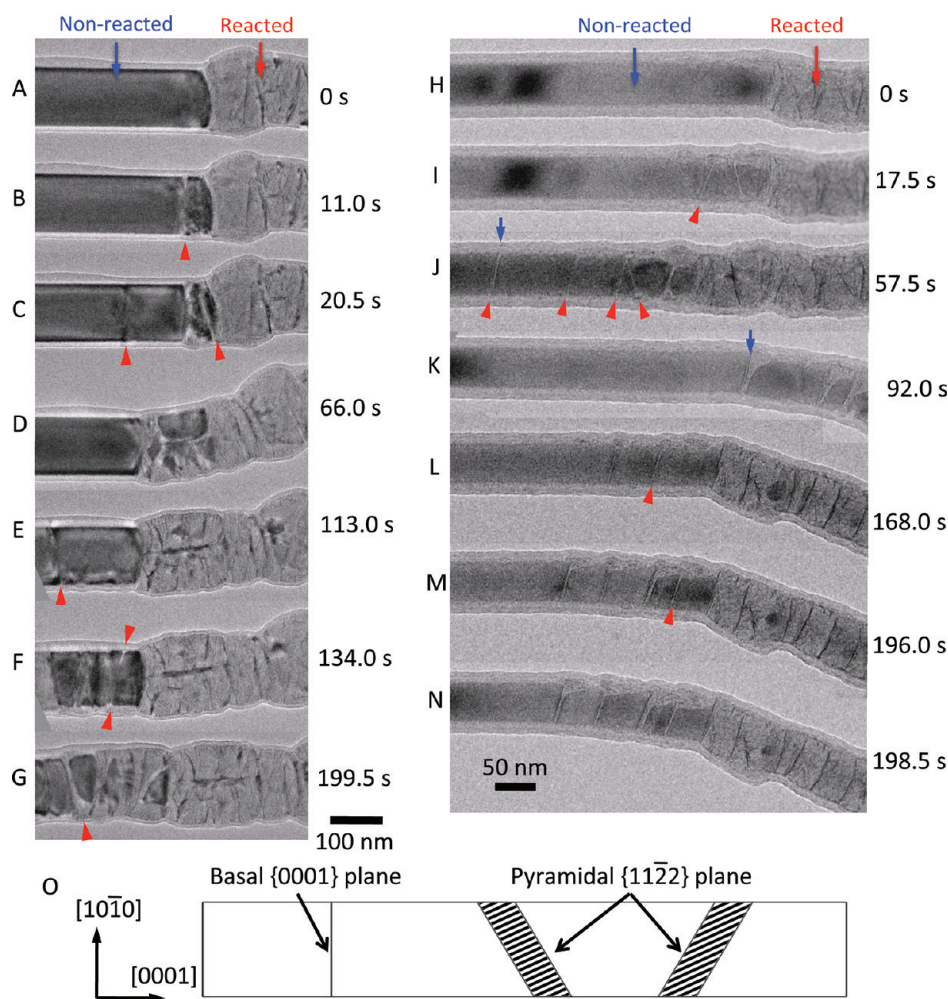
Figure 1. Discrete crack nucleation ahead of the reaction front (A−G and H−N). A−G and H−N are the lithiation processes for two different nanowires, respectively. See also Supporting Information movies SI2 and SI3. Cracks formed near the reaction front in the nonreacted part of the ZnO NW as indicated by the triangles in the figure separating the NW into multiple segments. These segments were lithiated individually from the crack inward to the bulk region. The volume expansion and the change in contrast indicate the segment is lithiated. After the NW was segmented (C), the segment was further subdivided into smaller domains (D,E). Penetration of the crack from the surface to the bulk region was observed in F. The arrows in J and K also point to cracks. After K, the NW was bent at the arrow. This is due to the uneven propagation of the reaction. Namely, one side of the wire was reacted faster than the other, causing larger volume expansion at one side of the wire and bending. (O) Basal and pyramidal planes in the ZnO NW.

electrodes and the possibility to improve battery performance, we are also interested in two basic materials science questions: (a) What, if any, are the microstructural precursors to ESSA? (b) The crystal → amorphous phase change in reaction 1 occurs by the motion of reaction front(s). Is a planar lithiation front stable (immune to fingering instability[16,17]) or not?

With respect to (a), in SnO_2 NWs dense clouds of glissile dislocations were seen to be generated and move right before the amorphization front,[9] which control NW shape transformation and relax the residual stress. SnO_2 bulk electrodes have comparatively better cyclability than ZnO bulk electrodes.[18] May the better cyclability of some ceramic electrodes be attributed to glissile dislocation generation and plastic deformation at the reaction front rather than cracking, even during the first lithiation (break-in) period? This is an important question, as "battery fading" is often due to the fracture and pulverization of electrode materials that break down the electron conduction pathways. The first lithiation could imprint an irreversible damage pattern that later grows. For (b), we know that most phase transformation

fronts can develop dynamic instabilities under appropriate conditions, such as the Mullins-Sekerka instability due to constitutional supercooling in alloy solidification, which breaks up a planar front. To have a good understanding of electrode cyclability, one must understand how the stress due to transformation is relieved by plasticity or fracture (as fracture is usually considered to be more damaging than plasticity), and how the residual stresses are distributed.

Our nanoscale electrochemical test consists of a single ZnO NW as an anode, an ionic-liquid electrolyte (ILE; lithium bis-(trifluoromethylsulfonyl)imide (LiTFSI) dissolved in 1-butyl-1-methylpyrrolidinium bis(trifluoromethylsulfonyl)imide (P_{14}TFSI)), and $LiCoO_2$ particles as cathode, a setup similar to that used in ref 9. After contacting the NW with ILE, a potential of −4.0 V with respect to the $LiCoO_2$ counter electrode was applied to the ZnO NW. The same bias voltage was used for all the charging experiments in this study unless otherwise stated. The solid-state reaction front propagated along the longitudinal direction of the NW away from the ILE. After charging, the reacted part was
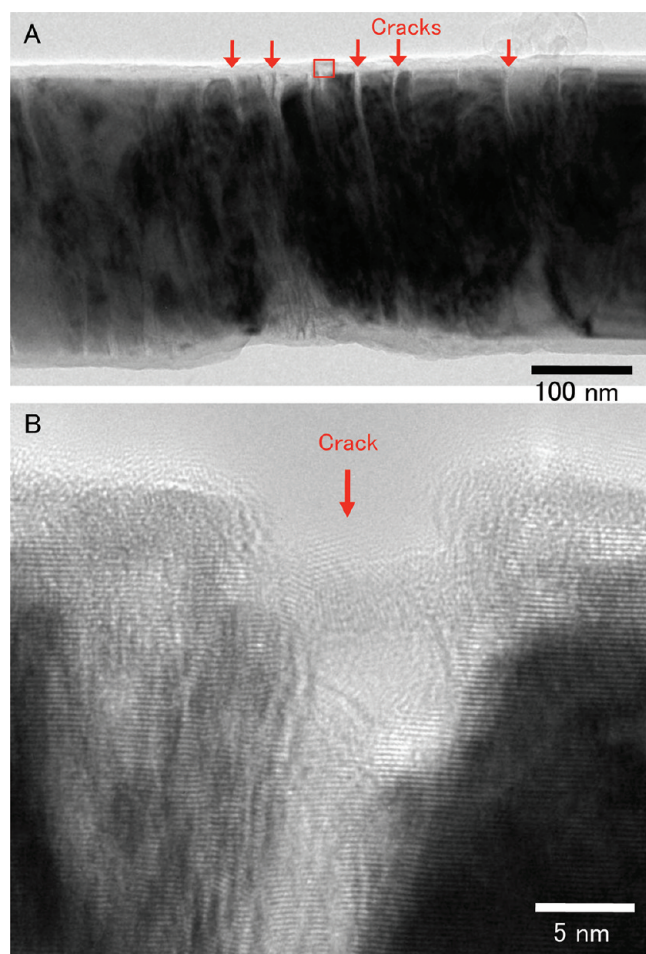
Figure 2. (A) The cracked ZnO NW at the early stage of lithiation. Cracks are indicated by the arrows. (B) The magnified view of the solid squared region in (A) showing clearly the formation of the crack.

elongated ~20% and the diameter expanded ~30%. The total volume expansion was estimated to be about ~100%.

Figure 1A–G (Supporting Information movie SI2) shows the propagation of the reaction front. A thin layer of ILE wicked up the NW surface after the NW contacted the ILE, with no clear sign of solid electrolyte interface (SEI). SEI was not observed in SnO_2 NW lithiation either, possibly because we are using ILE rather than the conventional (ethylene carbonate or dimethyl carbonate) electrolyte.[9] In contrast to SnO_2 NWs[9] where high density of glissile dislocations were nucleated with apparent dislocation plasticity, no dislocation was ever seen in the crystalline ZnO near the lithiation front (Figure 1A). Stress should be high, however, since we see the rapid evolutions of pseudomoiré TEM contrast ~100 nm ahead of the reaction front (Supporting Information movie SI3), which indicate large local bending and lattice strain. Strikingly, the reaction front did not move continuously. Instead, it leaped forward by initiating discrete cracks about 70 nm before the reaction front (Figure 1B, red arrowheads), followed by rapid Li^{+} surface diffusion along the open crack surfaces and inward amorphizations. The amorphous zone then grew until it met with the main reaction front (Figure 1C,D). During the process, new cracks emerged in the divided segment (Figure 1C, arrowheads), further subdividing it into smaller domains

(Figure 1D), which then were quickly lithiated (Figure 1E). This intriguing process then repeated itself (Figure 1F,G).

During the lithiation, volume expansion did not occur uniformly. The reacted NW surface was rough with undulating surface relieves (Figure 1), and the reacted NW bent upward (Figure 1A–D) or downward (Figure 1E–G). These features were seen in all of the NWs investigated. Another example is Figure 1H–N (Supporting Information movie SI3), which shows the discrete hopping of multiple cracks ahead of the reaction front. Three to five cracks were generated (Figure 1H–J, L-N), segmenting the nanowire, which were then lithiated simultaneously. It is noteworthy that the cracks were either perpendicular or inclined 16° to the NW axis. The NW growth direction is [0001] and the images in Figure 1 are viewed from [1$\bar{2}$10] direction. Therefore, the cracks observed are along pyramidal {11$\bar{2}$2} and basal {0001} planes as schematically shown in Figure 1O. Because these planes are the close-packed planes as well as slip planes in a wurzite crystal, the "lines" observed could be slip traces instead of cracks. However, high-resolution image at the intersection between the "line" and the NW surface clearly shows a crack instead of slip offset (Figure 2).

Lithiation transformed the initially straight ZnO NW (Supporting Information Figure S1A) into a curved and segmented structure with obvious radial expansion (Supporting Information Figure S1B). The diffraction pattern before the lithiation indicates the NW was a single crystal (Supporting Information Figure S1C). After lithiation, the pattern changed to diffraction spots superimposed on an amorphous halo (Supporting Information Figure S1D), indicating the formation of Li_xZn and ZnO nanocrystals dispersed in an amorphous Li_2O matrix, similar to the lithiation product of SnO_2 nanowires. Low-loss electron energy loss spectroscopy (EELS) after the lithiation confirmed the presence of Li_2O (Supporting Information Figure S1E). After a surface crack opened, ESSA propagated inward following the crack due to rapid Li^{+} diffusion along the two crack surfaces. When two growing amorphous regions came into contact and merged, they formed a new interface between them with TEM contrast (dark stripes in Figure 1). This is a glass–glass interface (GGI), as the two glassy domains had developed separately and were atomic-structurally discontinuous when they met and adhered. Thus the lithiated ZnO NW can be referred to as nano-amorphous or a nanoglass,[19] as it contains multiple atomic-structurally discontiguous glassy nanodomains. Also, the two glassy domains may not conform to each other perfectly, and voids or excess free volume could be trapped inside the GGI although our TEM could not resolve them. A high-resolution image near the GGI is shown in Supporting Information Figure S1F. The lattice fringe at the dark stripes corresponds to (0002) planes of ZnO, which indicates that the GGIs could contain some residual ZnO, while the light-colored areas are a mixture of LiZn crystals and the amorphous Li_2O. With physical aging of a nanoglass, the glass–glass interface should become delocalized over time by atomic structure rearrangements and disappear eventually. However, our experiments did not provide enough time and thermal activation and the GGIs remained localized during experimental observations. Indeed, the GGIs were also stable and persist at the same locations after multiple charge/discharge cycles later (see Figure 3), which we call "GGI memory effect". Thus, the damages trapped in GGIs in battery electrodes could be permanent, and studying how they form and their elementary properties should be important for understanding battery lifetimes.
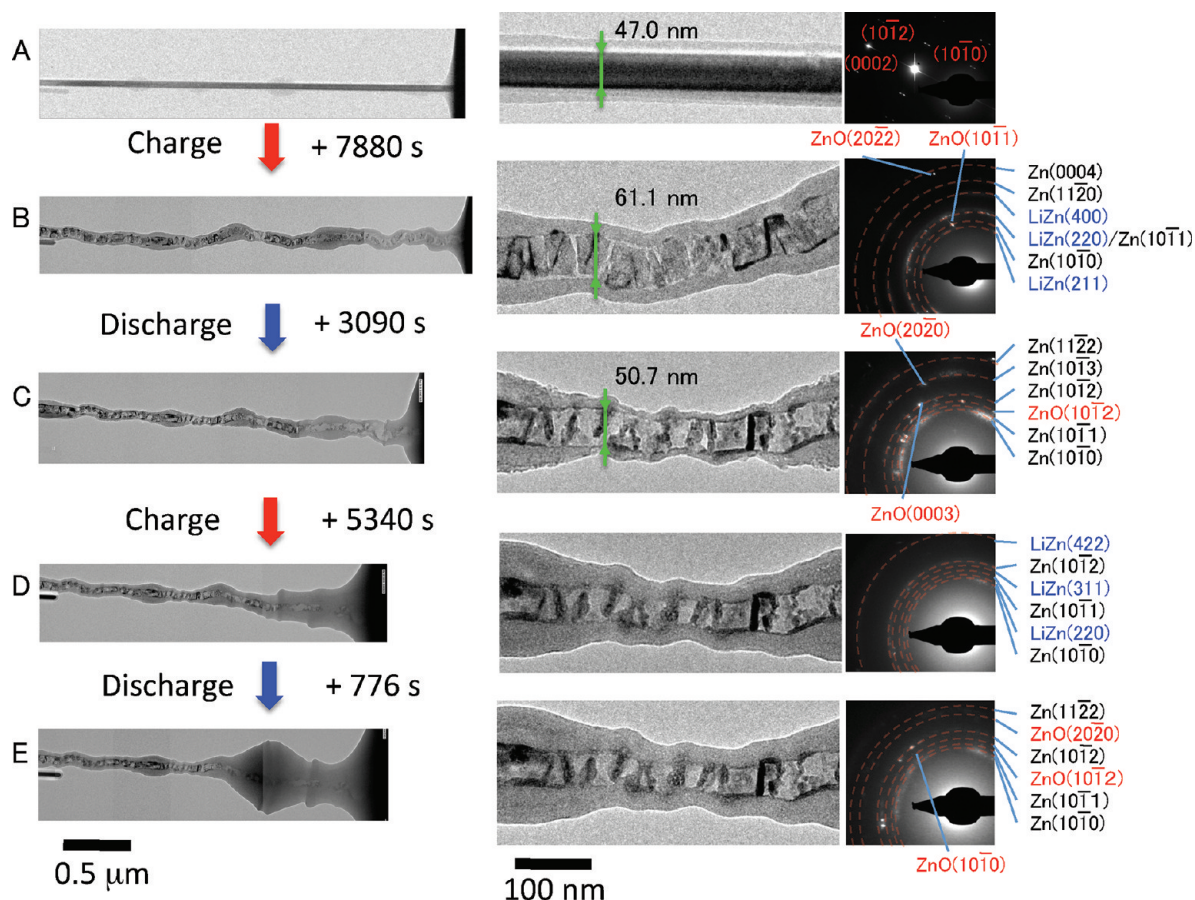
Figure 3. (A−E) Charge/discharge cycles. Left, middle, and right panels indicate low-magnification images, high-magnification images, and electron diffraction patterns, respectively. During the first lithiation process (A−B), the straight NW (A) was curved and segmented to multiple domains (B) and the diameter expanded from 47.0 to 61.1 nm. The change in the diffraction pattern indicates the formation of Zn and LiZn alloy. The diffraction pattern also shows the amorphous halo. After the delithiation (C), the NW reduced its diameter from 61.1 to 50.7 nm. The diffraction pattern shows that the LiZn alloy was converted to metallic Zn in the process. The NW remained segmented to multiple domains after the delithiation. The change in the NW volume was less obvious after the second lithiation and delithiation processes although the diffraction pattern showed the conversion of Zn and ZnO to Li_2O and LiZn alloy in the charging and LiZn alloy to Zn in the delithiation. The increasing intensity of the amorphous haloes in the lithiation/delithiation cycle implies the increase of the amorphous Li_2O in the NW. As a result, the NWs become less reactive to Li under lithiation and only small volume change was observed. This can also be a reason for the poor cyclability.

The results above were obtained by lithiating ZnO NWs with only tip of the NW contacting ILE. However, in actual battery configurations the electrodes are immersed in the liquid electrolyte. To investigate the effect of the ILE contact configuration, we conducted the following experiments with large part of the NWs immersed in the ILE. Generally speaking, the results (see Supporting Information Figure S2) are similar to the tip-contacted configuration. Because clarifying the fracture mechanism is critical for the design of LIB electrodes, detailed characterization of the initial crack formation were also performed. ZnO NW with length of 4.3 μm and diameter of 320 nm (Figure 4A) was immersed in the ILE and then a bias voltage of −4.0 V was applied. When the NW was extracted, the formation of cracks was observed at the solid square in Figure 4C. The magnified view of the area is shown in Figure 4D. No apparent volume expansion was observed at this point. Therefore, we confirmed that the NW was in the initial stage of the lithiation just after the crack formation. Electron energy-loss spectroscopy mapping showed the enhanced presence of Li in the crack (Figure 4E, the same area as shown in Figure 4D), proving that the Li$^+$ penetrated inside the NW through the crack. The high-resolution images of

the NW before and after the reaction are shown in Figure 4F,H, respectively (the electron diffraction pattern in Figure 4G indicates the growth direction of the NW was ⟨0001⟩). The volume expansion and the change in the contrast were observed at the intersection between the crack and the NW surface as indicated by the dashed circle. Note that the NW remained nonreacted outside of the circle in Figure 4H, indicating that Li was not adsorbed uniformly on the ZnO NW at least in the early stages, and the lithiation initiated preferentially from surfaces where there is large free volume. Since the complete lithiation of ZnO requires volume expansion ∼100%, high tensile stresses (both longitudinal and hoop) must be created at the surface, causing the NW to crack from the surface. While the initial cracks were cross-sectional (likely due to crystallography) driven by the longitudinal tensile stress, we do see radial crack nucleation and growth driven by the tensile hoop stress in Figures 1D and 4, and Supporting Information movie SI2, causing the further subdivision of the segmented nanowire. Also, ab initio calculations below indicate that Li embrittlement in ZnO plays a huge role in assisting the crack formation. Nevertheless, in our experiments we did not observe complete fracture, that is, breaking into two
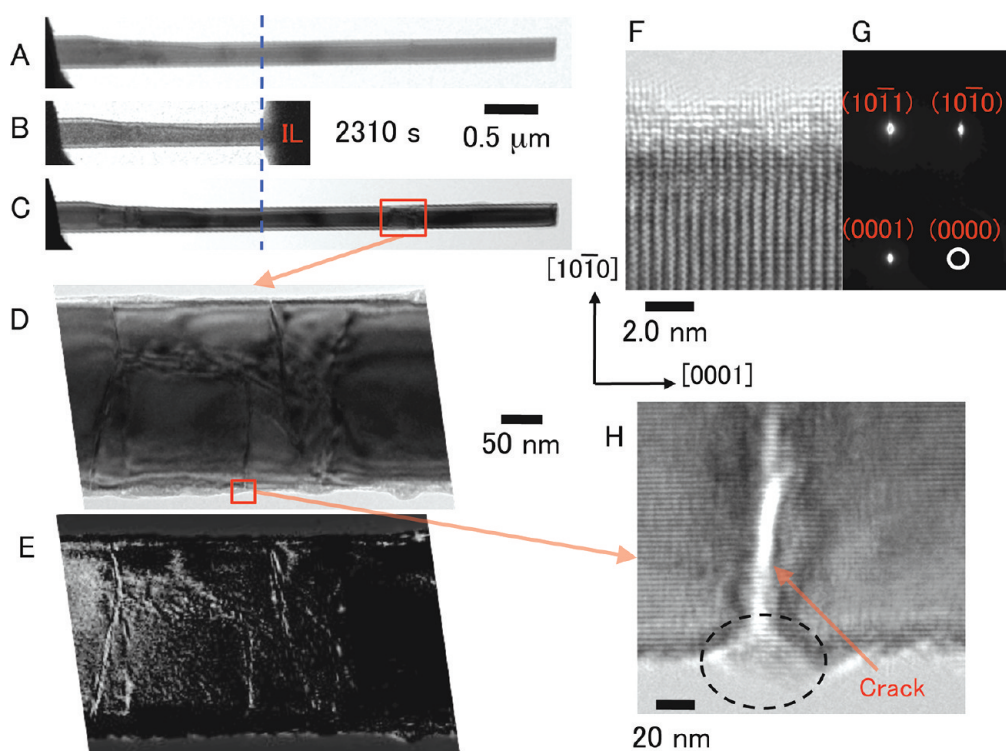
Figure 4. Early stage of the crack formation in ZnO NW during lithiation. The pristine ZnO NW (A) was immersed into the IL and the bias voltage of −4.0 V was applied to the system for 2310 s (B). Then the NW was extracted from the IL (C). Panel D is the magnified view at the solid square in panel C. The NW possessed cracks without clear sign of the volume expansion indicating the bulk region remained unreacted. Panel E is the Li mapping where the high Li concentration region is shown in white. (F) High-resolution image of the ZnO NW before lithiation. The diffraction image (G) indicates the growth direction was [0001]. (H) Magnified view of the crack tip at the region marked with the solid square in panel D. The surface remained nonreacted except at the intersection between the crack and the surface as indicated by the dashed circle.

pieces, of the NWs despite the crack formations. This is because (a) mechanically, the stress integral along any cut of the NW must be zero for a free-standing NW and thus the tensile normal stress that opens the mode-I crack must be balanced by compressive normal stress further along the crack path, preventing catastrophic crack growth. (This would be different if the NW is not free-standing, like a NW in an aggregate) and (b) the crack formation was immediately followed by Li penetration and the lithiation product filled the crack with the volume expansion, which then adheres and glues the segments mechanically together.[20,21]

Figure 5 summarizes the leapfrog cracking and nanoamorphization process, which occurs by the following steps in our ZnO system:

1) The surface of the NW is lithiated, which induced large tensile stresses near the surface.

2) Surface cracks nucleate in the NW and propagate along $\{0001\}$ or $\{11\bar{2}2\}$ cleavage planes.

3) Li$^+$ diffuse along the crack surfaces and then penetrate inward, causing amorphization.

4) The two amorphous regions grow separately and eventually meet and adhere with each other, forming a glass/glass interface (GGI), by the reaction

$$\text{Glass Surface 1} + \text{Glass Surface 2} \rightarrow \text{GGI Type I} \qquad (2)$$
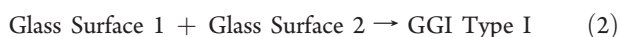
5) The remaining crystal continues to shrink. Eventually, two moving crystal/glass interfaces (CGIs) will meet, forming another GGI by the reaction

$$\text{CGI 1} + \text{CGI 2} \rightarrow \text{GGI Type II} \qquad (3)$$
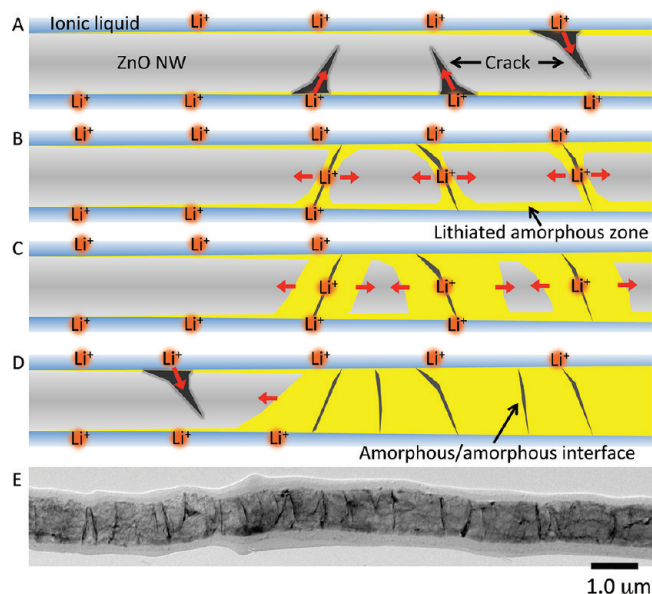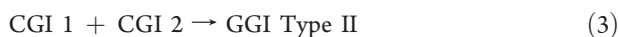
Figure 5. (A−D) Schematic illustration explaining the leapfrog cracking and nanoamorphization lithiation mechanism of ZnO NWs. The lithiation first took place at the surface of the NW. The volume expansion and stress then induced cracking from the surface toward the core. Then, Li$^+$ rapidly penetrated inside the NW along the crack by surface diffusion, followed by separate amorphization perpendicular to the crack surfaces. During the lithiation, the region where two growing amorphous domains met became amorphous/amorphous interface, turning ZnO NW into a nanoglass. As a result, the NW was separated into multiple nano amorphous segments after the lithiation (E).
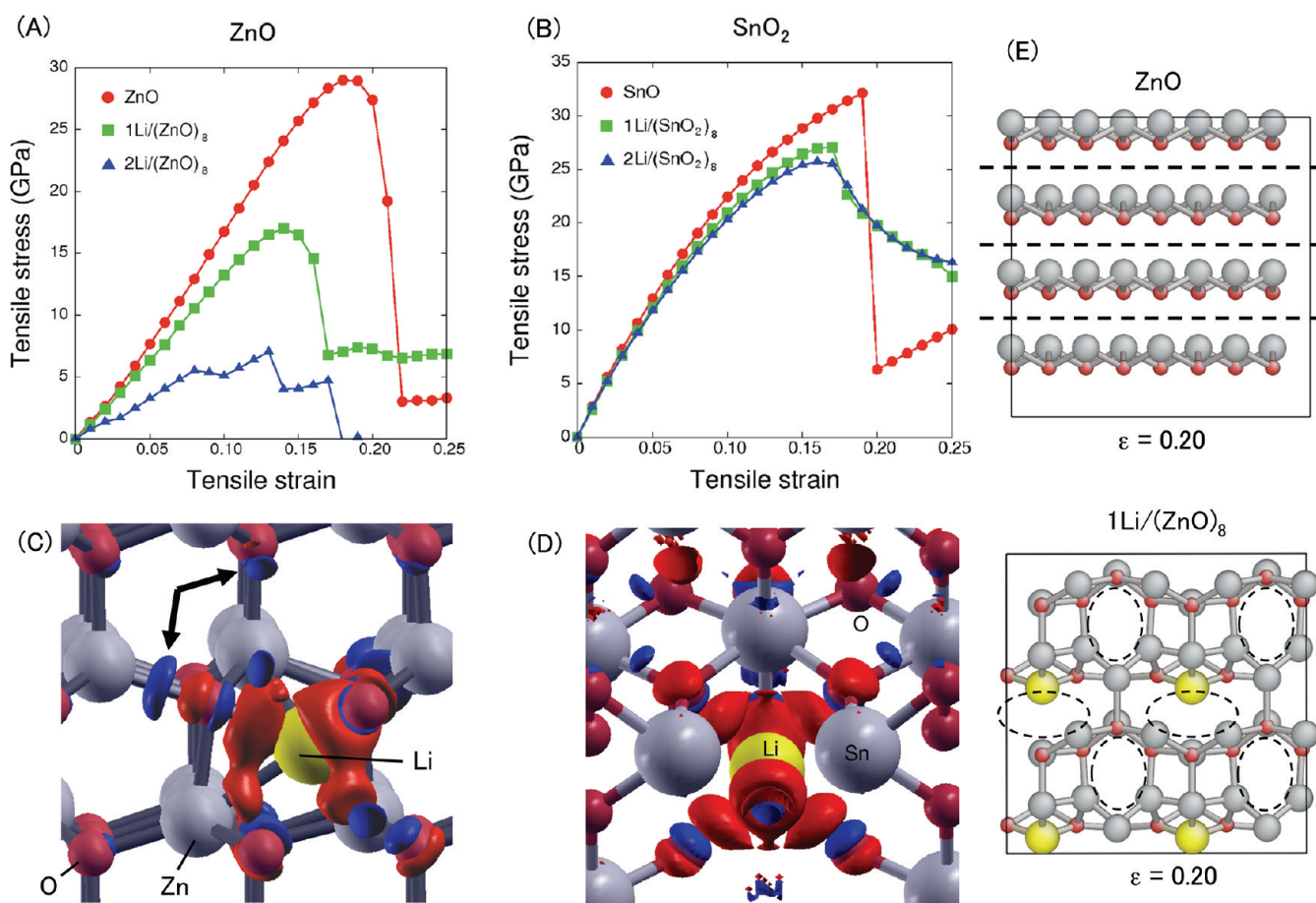
Figure 6. (A) The tensile stress—strain curve of the bulk ZnO w/o Li (circles), w/Li at the concentration ratio of $1Li/(ZnO)_8$ (squares), and $2Li/(ZnO)_8$ (triangles). (B) The tensile stress—strain curves of the bulk SnO_2 w/o Li (circles, w/Li at the concentration ratio of $1Li/(SnO_2)_8$ (square) and $2Li/(SnO_2)_8$ (triangles). (C) Change in electron density distribution after Li insertion of ZnO and (D) SnO_2. The iso-surfaces indicating the density change of $+0.015$ Å^{-3} and -0.015 Å^{-3} are the red and the blue surfaces, respectively. (E) Change in the atom structures of the intrinsic ZnO and $1Li/(ZnO)_8$ model. The $2 \times 2 \times 2$ units of the simulation cell are drawn in the figure so that the bond breaking (dashed lines) and the void formation (dashed circles) are clear.

The above 1—5 process divides the NW into multiple segments, creating a nanoglass after the lithiation (Figure 5E). Whether or not further subdivisions will happen after segmental division seems to depend on the NW diameter: radial cracking occurs more frequently in Figure 1A—G (Supporting Information movie SI2), causing further subdivision, than in Figure 1H—N (Supporting Information movie SI3), because the latter NW is thinner.

The cracking cannot be simply due to the large volume expansion, since SnO_2 NWs sustain even larger volume expansion under the same experimental setup, but usually did not crack.[9] The Li/Zn chemistry must play a role. Like hydrogen embrittlement, previous studies have shown the presence of Li can greatly reduce the mechanical strength of materials, known as lithium embrittlement.[22−26] To elucidate the effect of Li on strength and ductility, we conducted ab initio simulations of ZnO and SnO_2 tensile decohesion using Vienna Ab Initio Simulation Package[27,28] (VASP). Details of the calculations are in Supporting Information. Figure 6A shows the tensile stress—strain curve of ZnO with different Li concentrations. The ideal strength of pure ZnO is 29 GPa. When Li was added, it decreased to 17 and 7 GPa for $1Li/(ZnO)_8$ and $2Li/(ZnO)_8$ concentration, respectively. In contrast, at the same ratios of Li/Sn, the effect on the tensile decohesion of SnO_2 is seen to be much smaller (Figure 6B). Thus lithium embrittlement is severe in ZnO, but slight in SnO_2.

We attribute this striking difference to the aliovalency of Sn cations; both Sn(IV) and Sn(II) are frequently occurring electronic valence states of Sn, while zinc chemistry is dominated by the Zn(II) state. Thus, when Li are inserted and started to reduce the original cations, Sn can adapt to this electronic-structure change more gradually, while Zn has no option but to break the Zn—O bond abruptly. This effect is illustrated by the electron density difference map calculated in Figure 6C,D, when a Li atom is inserted into the crystalline ZnO or SnO_2. The red and blue isosurfaces indicate density change of $+0.015$ eÅ^{-3} and -0.015 eÅ^{-3} compared to the pure ceramic, respectively. In the case of ZnO (Figure 6C), the density differences were concentrated between Li and its first neighbor O atoms, and as a result the electron density is reduced at the Zn—O bond as indicated by the arrows. This causes the bonds to severely weaken after lithiation. The effect of this bond weakening became evident as the tensile strain was applied. Figure 6E shows the change in the atomic structure of ZnO after the fracture comparing the pure ZnO and $1Li/(ZnO)_8$ model. In pure ZnO, the Zn—O bond along the tensile strain was equally stretched and broke along the dashed lines after reaching the maximum stress. On the other hand, voids were formed in the regions marked by the dashed circles for $1Li/(ZnO)_8$ model. This is because the inserted Li attracted the surrounding electrons to weaken Zn—O bonding. In contrast, in

the case of SnO$_2$ (Figure 6D), the changes in the bonding charge density along Sn−O bonds are significantly smaller, leading to only slight changes in the decohesion strength (Figure 6B). Thus, just as our experiments suggested, lithium embrittlement is much more severe in ZnO than in SnO$_2$, and as a result the electrochemically driven solid-state amorphization[11] of ZnO is preceded by nanocracking rather than dislocation plasticity. Nanocracking is the direct cause of nanoamorphization and the damage patterns resident in Figures 1G,N and 4E configurations, which persist even after multiple charge/discharge cycles (Figure 3), in contrast to the single glassy domain and smooth product surface in the case of SnO$_2$.[9]

Although the possibility of lithium embrittlement in LIB casings was speculated from the observation of lithium battery leakage,[29] there had been no extensive research in this direction. Our findings shed light on the importance of nanofracturing and lithium embrittlement in LIB electrodes, since they are integral to the lithiation mechanism, as well as battery decrepitation mechanisms. While it is known that the charge/discharge cycle in LIB leads to a capacity loss[30] attributed to the large volume change and cracking,[31] our work shows real-time TEM observation of the crack formation during the electrochemical cycles and contrasts it and its aftermath to the dislocation plasticity mechanism that leads to more ductile accommodation in SnO$_2$.[9] We also show that electrochemical reaction can be another method to synthesize nanoglass in addition to the original inert gas condensation method.[19,32,33] The glassy nanodomain size and free volume distribution inside the nanoglass may be tuned by annealing or changing the reaction voltage, which expands the possibility of material design for tunable properties.[34]

ASSOCIATED CONTENT

Ⓢ Supporting Information. Additional information, figures, and movies. This material is available free of charge via the Internet at http://pubs.acs.org.

AUTHOR INFORMATION

Corresponding Author
*E-mail: (J.L) liju@seas.upenn.edu; (J.Y.H) jhuang@sandia.gov.

ACKNOWLEDGMENT

REFERENCES

(1) Chan, C. K.; Peng, H.; Liu, G.; McIlwrath, K.; Zhang, X. F.; Huggins, R. A.; Cui, Y. *Nat. Nanotechnol.* **2008**, *3*, 31.

(2) Magasinski, A.; Dixon, P.; Hertzberg, B.; Kvit, A.; Ayala, J.; Yushin, G. *Nat. Mater.* **2010**, *9*, 353.

(3) Park, M. -S.; Wang, G.-X.; Kang, Y. -M.; Wexler, D.; Dou, S.-X.; Liu, H.-K. *Angew. Chem., Int. Ed.* **2007**, *46*, 750.

(4) Ko, Y. -D.; Kang, J.-G.; Park, J.-G.; Lee, S.; Kim, D. -W. *Nanotechnology* **2009**, *20*, 455701.

(5) Kim, H.; Cho, J. *Nano Lett.* **2008**, *8*, 3688.

(6) Nam, K. T.; Kim, D.-W.; Yoo, P. J.; Chiang, C.-Y.; Meethong, N.; Hammond, P. T.; Chiang, Y.-M.; Belcher, A. M. *Science* **2006**, *312*, 885.

(7) Bhandakkar, T. K.; Gao, H. *Int. J. Solids Struct.* **2010**, *47*, 1424.

(8) Zhu, T.; Li, J. *Prog. Mater. Sci.* **2010**, *55*, 710.

(9) Huang, J. Y.; Zhong, L.; Wang, C. M.; Sullivan, J. P.; Xu, W.; Zhang, L. Q.; Mao, S. X.; Hudak, N. S.; Liu, X. H.; Subramanian, A.; Fan, H.; Qi, L.; Kushima, A.; Li, J. *Science* **2010**, *330*, 1515.

(10) Mai, L. Q.; Dong, Y. J.; Xu, L.; Han, C. H. *Nano Lett.* **2010**, *10*, 4273.

(11) Limthongkul, P.; Jang, Y.-I.; Dudney, N. J.; Chiang, Y.-M. *Acta Mater.* **2003**, *51*, 1103.

(12) Liu, J.; Li, Y.; Ding, R.; Jiang, J.; Hu, Y.; Ji, X.; Chi, Q.; Zhu, Z.; Huang, X. *J. Phys. Chem. C* **2009**, *113*, 5336.

(13) Li, H.; Huang, X.; Chen, L. *Solid State Ionics* **1999**, *123*, 189.

(14) Belliard, F.; Connor, P. A.; Irvine, J. T. S. *Solid State Ionics* **2000**, *135*, 163.

(15) Wang, H.; Pan, Q.; Cheng, Y.; Zhao, J.; Yin, G. *Electrochim. Acta* **2009**, *54*, 2851.

(16) Mullins, W. W.; Sekerka, R. F. *J. Appl. Phys.* **1964**, *35*, 444.

(17) Cross, M. C.; Hohenberg, P. C. *Rev. Mod. Phys.* **1993**, *65*, 851.

(18) Connor, P. A.; Belliard, F.; Behm, M.; Tovar, L. G.; Irvine, J. T. S. *Ionics* **2002**, *8*, 172.

(19) Gleiter, H. *MRS Bull.* **2009**, *34*, 456.

(20) Li, C.-F. *J. Power Sources* **2011**, *196*, 768.

(21) Courtney, I. A.; Dahn, J. R. *J. Electrochem. Soc.* **1997**, *144*, 2045.

(22) Dey, A. N. *J. Electrochem. Soc.* **1971**, *118*, 1547.

(23) Vertkov, A. V.; Evtikhin, V. A.; Lyublinskii, I. E.; Sychev, A. A. *Mater. Sci.* **1990**, *26*, 153.

(24) Old, C. F. *J. Nucl. Mater.* **1980**, *92*, 2.

(25) Boothby, R. M. *J. Nucl. Mater.* **1992**, *186*, 209.

(26) Shunk, F. A.; Warke, W. R. *Scr. Metall.* **1974**, *8*, 519.

(27) Kresse, G.; Hafner, J. *Phys. Rev. B* **1993**, *47*, 558.

(28) Kresse, G.; Furthmüller, J. *Phys. Rev. B* **1996**, *54*, 11169.

(29) Balakrishnan, P. G.; Ramesh, R.; Prem Kumar, T. *J. Power Sources* **2006**, *155*, 401.

(30) Weydanz, W. J.; Wohlfahrt-Mehrens, M.; Huggins, R. A. *J. Power Sources* **1999**, *81−82*, 237.

(31) Tamura, N.; Ohshita, R.; Fujimoto, M.; Kamino, M.; Fujitani, S. *J. Electrochem. Soc.* **2003**, *150*, A679.

(32) Jing, J.; Krämer, A.; Birringer, R.; Gleiter, H.; Gonser, U. *J. Non-Cryst. Solids* **1989**, *113*, 167.

(33) Gleiter, H. *J. Appl. Crystallogr.* **1991**, *24*, 79.

(34) Gleiter, H. *Acta Mater.* **2008**, *56*, 5875.

Supporting Information

(SI1) Descriptions of TEM setup, sample preparation, and *ab initio* calculation. Supplementary figures S1 and S2.

(SI2) An in-situ TEM movie showing the leapfrog cracking and nano-amorphization of ZnO nanowire during electrochemical lithiation. Discrete cracks were initiated 50-150 nm ahead of the main reaction front. The video was recorded at 2 frames/s, and played at 10× speed.

(SI3) An in-situ TEM movie showing the leapfrog cracking and nanoamorphization of ZnO nanowire during electrochemical lithiation. Discrete cracks were initiated 20-200 nm ahead of the main reaction front. The video was recorded at 2 frames/s, and played at 10× speed.

SUPPORTING INFORMATION (SI1)

TEM setup and sample preparation: Our experiments were conducted inside a FEI Tecnai F30 field emission gun transmission electron microscope (TEM) using a Nanofactory TEM-scanning tunneling microscopy (STM) holder. The TEM was operated at 300 kV, with a point-to-point resolution around 0.2 nm. The videos containing lithiation process were recorded by a CCD (charge-coupled device) camera at 2 frames per second.

ZnO nanowires (NWs) used in this work were grown on either carbon cloth or Si wafer by vaporization and condensation technique described in Refs. (1-3). In both cases, a mixture source of ZnO powder (Alfa Aesar, 99.9%) and graphite powder (Alfa Aesar, 99.9%) was placed at the higher temperature zone and the carbon cloth or Si wafer was placed in the lower temperature zone of a horizontal tube furnace. The furnace was heated to 900 - 1100 °C using argon as the carrier gas. The deposition of the vapor phase on a carbon cloth or silicon substrate located at down stream formed the nanowires.

Ab initio calculations: For ZnO, the tensile strain was applied to the <001> direction corresponding to the axial direction of the NW. A 6.51 Å × 5.64 Å × 5.25 Å unit cell of wurzite ZnO including 8 Zn and 8 O atoms was used. The crystallographic orientations of the simulation cell are $[10\bar{1}0]$, $[1\bar{2}10]$, and [0001] in x, y, and, z direction, respectively. We employed density functional theory formalism with generalized gradient approximation parameterized by Perdew, Burke and Ernzerhof[4] using planewave basis set. The ionic cores were represented with projector-augmented wave potentials.[5,6] An energy cutoff of 400 eV was chosen for the expansion of the plane wave function and a 3 × 4 × 4 Monkhorst-Pack[7] k-point mesh was selected in the simulations. First, the atomic configurations and the cell vectors were relaxed to minimize the total energy of the single crystal ZnO system. Then the tensile strain was applied to the model by elongating the simulation cell along z direction with the increment of 0.01. After the each increment of the strain, the structural optimization was performed while fixing the cell size in z direction. Two different Li concentration ratios were considered ($1Li/(ZnO)_8$ and $2Li/(ZnO)_8$). The Li atoms were added to the ZnO at the octahedral interstitial sites,[8] and the Li atoms were placed as far away as possible to each other for $2Li/(ZnO)_8$ model. For SnO_2, a 6.75 Å × 6.75 Å × 6.45 Å unit cell of rutile including 8 Sn and 16 O atoms was used. The crystallographic orientations of the simulation cell are [110], $[1\bar{1}0]$, and [001] in x, y, and, z direction, respectively. A 4 × 4 × 4 Monkhorst-Pack[7] k-point mesh was selected in the simulations. All other conditions were the same as in the ZnO calculation.
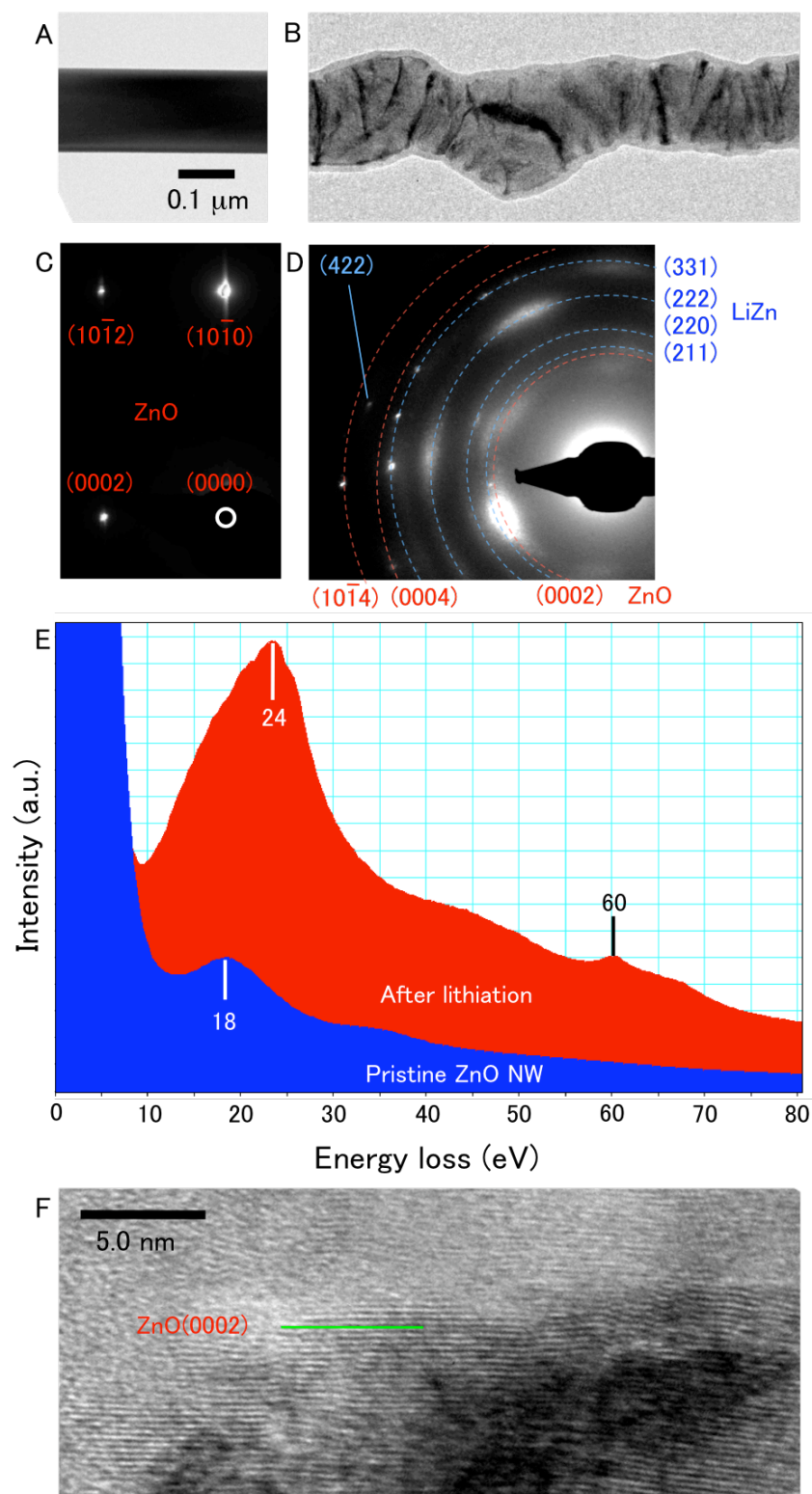
Figure S1. The ZnO NW (A) before and (B) after lithiation. The initial straight NW was curved and segmented by the dark stripes after the reaction. Diffraction patterns of the ZnO NW (C) before and (D) after lithiation. The d-spacings of ZnO and LiZn are shown in red and blue, respectively. The diffraction pattern after the lithiation also shows the amorphous halo. (E) Low-loss electron energy loss spectroscopy (EELS) from large area of the NW after reaction (red profile) and a pristine NW (blue profile). The plasmon loss peaks at 18 eV and 24 eV are in agreement with ZnO and Li_2O. Peak at 60 eV indicates the presence of Li. (F) The high-resolution image of the lithiated ZnO NW near the dark stripe. The lattice spacing at the stripe corresponds to (0002) planes of ZnO.
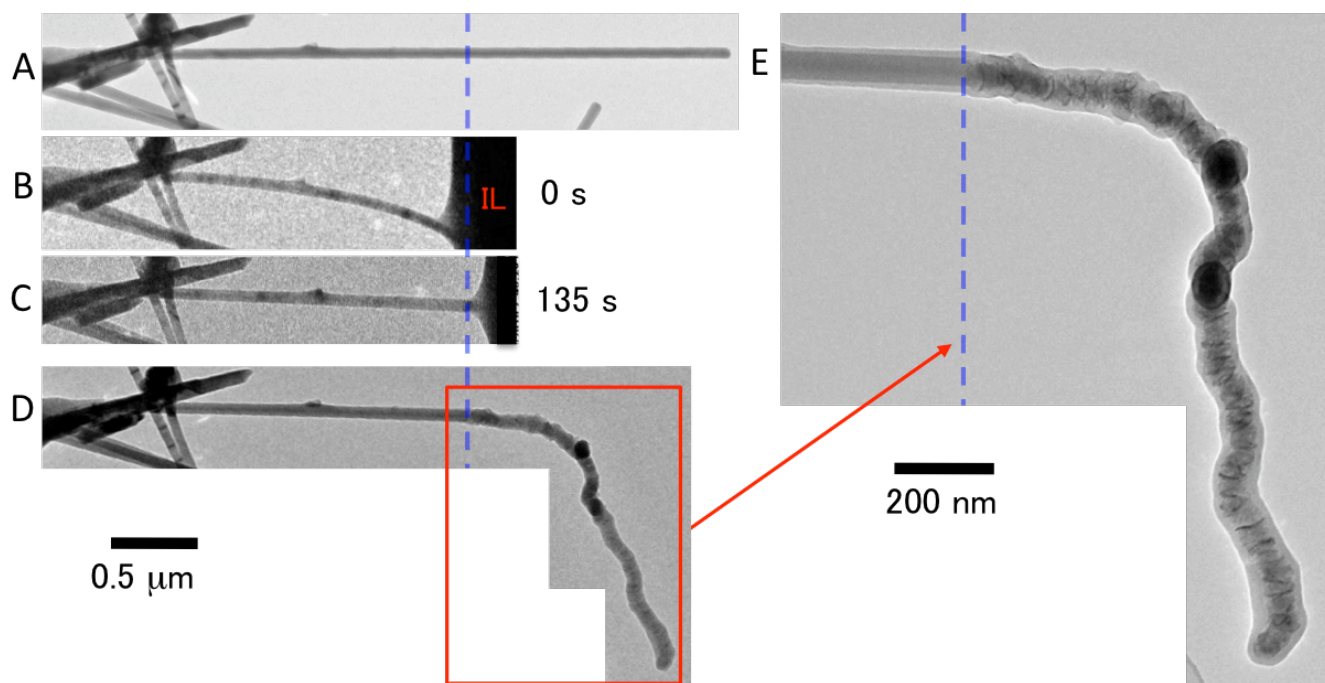
Figure S2. The lithiation process of the ZnO NWs immersed in the ILE. The diameter of the NW is 62.5 nm. First, the NW was immersed in the ILE. Then, a bias voltage of -4.0 V with respect to the cathode was applied to the NW anode. After 135 s, the NW was extracted from the ILE and the structure of the reacted part of the NW was inspected. The dashed line indicates the surface of the ILE when the NW was immersed in the ILE. The reacted part of the NW was segmented to multiple "nanoamorphous grains" as shown in Fig. S1E. The reaction mechanism was the same as the one observed in the experiments with only the tip of the NW touching the ILE. This implies the lithiation mechanism does not depend on the contact configuration. Although we were unable to observe crack formation in the immersed part of the NW due to the surrounding thick ILE layer, the segmented morphology of the reacted NW implies that the Li^+ was inserted to the NW through the crack even when the NW was immersed in the ILE.

References

(1)   Banerjee, D.; Lao, J. Y.; Wang, D. Z.; Huang, J. Y.; Steeves, D.; Kimball, B.; Ren, Z. F.; Sennett, M. *Appl. Phys. Lett.* **2003**, 83, 2061.

(2)   Banerjee, D.; Lao, J. Y.; Wang, D. Z.; Huang, J. Y.; Steeves, D.; Kimball, B.; Ren, Z. F. *Nanotechnology* **2004**, 15, 404.

(3)   Pan, Z. Y.; Dai, Z. R.; Wang, Z. L. *Science* **2001**, 291, 1947.

(4)   Perdew, J. P.; Burke, M. K. Ernzerhof, *Phys. Rev. Lett.* **1996**, 77, 3865.

(5)   Kresse, G.; Joubert, D. *Phys. Rev. B* **1999**, 59, 1758.

(6)   Blöchl, P. E. *Phys. Rev. B* **1994**, 50, 17953.

(7)   Monkhorst, H. J.; Pack, J. D. *Phys. Rev. B* **1976**, 13, 5188.

(8)   Huang, G. -Y.; Wang, C. -Y.; Wang, J. -T. *J. Phys: Condens. Matter* **2009**, 21, 345802.